

# Cool windows: simultaneously engineering high visible transparency and strong solar rejection

*Yeonghoon Jin,<sup>1,2,#</sup> Seungwon Kim,<sup>1,#</sup> Tanuj Kumar,<sup>2</sup> Mikhail A. Kats,<sup>2\*</sup> and Kyoungsik Yu<sup>1,\*</sup>*

<sup>1</sup>School of Electrical Engineering, Korea Advanced Institute of Science and Technology (KAIST), Daejeon 34141, Republic of Korea

<sup>2</sup>Department of Electrical and Computer Engineering, University of Wisconsin-Madison, Madison, WI 53706, USA

<sup>#</sup>These authors contributed equally

E-mail: [mkats@wisc.edu](mailto:mkats@wisc.edu), [ksyu@kaist.edu](mailto:ksyu@kaist.edu)

Keywords: transparent coolers, radiative cooling, emissivity, thin films

## Abstract

For window applications in hot climates, it is desirable to have windows with high visible transparency, while maintaining strong reflectance in both the ultraviolet and near infrared, to minimize unwanted heat gain. Given that more than 70% of incident solar energy is at wavelengths shorter than 1000 nm, achieving spectrally abrupt transitions from transparent to reflecting at the boundaries of the visible is essential. Such abrupt transitions at multiple wavelengths typically would require tens of dielectric layers, which is impractical for most window applications. Here, we propose and realize a structure comprising only eight planar layers that achieves sharp reflectance changes at ~390 and ~680 nm, resulting in high visible transmittance (>70%), and high near-infrared (>80%) and UV (>60%) reflectance, as well as high mid-infrared emissivity (>90%) for additional radiative cooling. We demonstrate an air temperature reduction of up to 3.8 °C with our engineered window compared to a reference window.

## Introduction

The inside of a car parked in sunlight on a hot summer day can quickly reach lethal temperatures, for example reaching 70 °C when the outside temperature is 40–45 °C.<sup>1</sup> This is because the windows form a greenhouse, passing most solar wavelengths while rejecting the mid-infrared thermal radiation that would otherwise enable cooling. The solar spectrum reaching the Earth’s surface has meaningful power for wavelengths from 300 nm to 2.5 μm, and nearly all but the shortest of these wavelengths are transmitted through typical windows.

In this paper, we aim to design a highly visible-transparent window for hot-weather operation. In particular, we aim to have sufficiently high transparency across 400–680 nm, along with high reflectance in the ultraviolet (300–400 nm) and the near-infrared (680–2500 nm) to prevent unwanted heating (**Figure 1b**). Notably, the highest near-infrared and near-UV intensities of sunlight are in the wavelength ranges just outside the visible, and therefore an abrupt change in optical reflectance at the visible boundaries (both 400 and 680 nm) is necessary to maximize heat rejection (**Figure 1b**).

Various strategies have been developed for visible-transparent infrared reflectors, such as a dielectric-metal-dielectric (DMD) configuration,<sup>2-5</sup> metallic nanostructures,<sup>6-7</sup> and indium-tin-oxide (ITO)-based structures,<sup>8-10</sup> however, such strategies often exhibit gradual changes in reflectance (*e.g.*, a DMD structure in **Figure 2a**), limiting the rejection of the unwanted portions of the solar spectrum. As shown in **Figure 1c**, the solar-spectrum-weighted infrared reflectance ( $R_{\text{IR}}$  at 680–2500 nm) of these nominally infrared-rejecting technologies in the literature (the filled symbols) is generally lower than 60~70%.

Recently, there have been attempts to demonstrate abrupt changes in reflectance and transmittance at the boundaries of the visible range.<sup>11-15</sup> For example, abrupt changes have been realized using a silver/silica multilayer stack,<sup>15</sup> and via a 30-layer dielectric stack,<sup>11</sup> in both cases resulting in high visible transmittance ( $T_{\text{vis}}$ ) and  $R_{\text{IR}}$  (the half-filled circles in **Figure 1c**). However, none of them demonstrated  $T_{\text{vis}} > 70\%$  and  $R_{\text{IR}} > 80\%$  simultaneously; we set the standard for  $T_{\text{vis}}$  at 70% because the visible transmittance for vehicle windshields must be higher than 70%, according to the U.S. National Highway Traffic Safety Administration.<sup>16</sup> Note that one structure gets close,<sup>11</sup> reporting  $T_{\text{vis}} \sim 78\%$  and  $R_{\text{IR}} \sim 77\%$ , but is composed of 30 dielectric layers, which is impractical for most window applications.

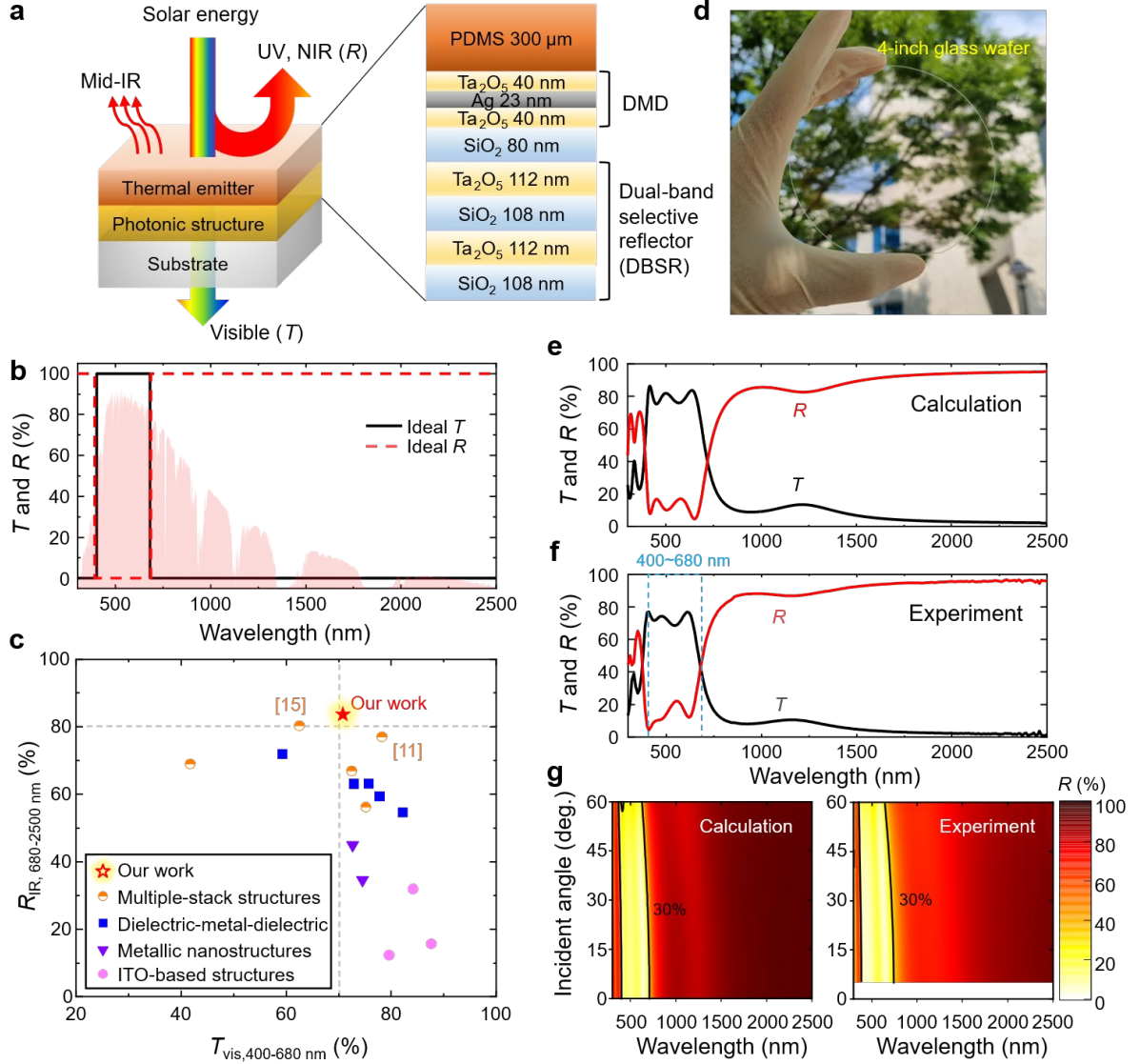


**Figure 1.** Optical design and properties of our photonic structure. **(a)** Schematic of the layered structure. **(b)** Transmittance ( $T$ ) and reflectance ( $R$ ) spectra of an ideal heat-rejection window. The red background is the solar spectrum (AM1.5). **(c)** Comparison of the solar-spectrum-weighted visible transmittance ( $T_{vis, 400-680 \text{ nm}}$ ) and IR reflectance ( $R_{IR, 680-2500 \text{ nm}}$ ) between our photonic structure and previous works. **(d)** A photo of our photonic structure, fabricated on a 4-inch glass, which shows its high visible transparency. **(e, f)** Calculated (e) and measured (f)  $R$  and  $T$  spectra. **(g)** Calculated (left) and measured (right) angle-dependent  $R$  spectra. The input light was assumed to be unpolarized.

Here, we propose and demonstrate a cool window coating that satisfies high  $T_{vis}$  ( $>70\%$ ) and  $R_{IR}$  ( $>80\%$ ) using just 8 layers. The structure of the coating is a combination of what we refer to as a dual-band selective reflector (DBSR), a dielectric-metal-dielectric (DMD) layer that provides long-wavelength ( $>1000 \text{ nm}$ ) reflectance, and a transparent layer of polydimethylsiloxane (PDMS) with high mid-infrared emissivity. The DBSR is a modified Bragg reflector with a photonic bandgap in the short-wavelength near-infrared (680–950 nm), that we have engineered to have a second photonic bandgap in the ultraviolet (350–400 nm), without increasing the number of layers or the overall structure thickness compared to the

conventional Bragg reflector (see Supporting Note S1). Our cool window shows an air temperature reduction inside an enclosure of as much as 3.8 °C compared to a reference piece of glass.

## Results

### Optical properties of our cool window

A schematic of our cool window is shown in **Figure 1a**, with a photo of a realization on a 4-inch glass wafer shown in **Figure 1d**, demonstrating high visible transparency. **Figure 1e** shows the calculated reflectance ( $R$ ) and transmittance ( $T$ ) spectra and **Figure 1f** shows the experimentally measured spectra. Abrupt changes in  $R$  and  $T$  can be observed around 390 and 680 nm, as desired for efficient heat rejection. The average transmittance in the visible (400–680 nm) range,  $T_{\text{vis}}$ , is ~71% and the average reflectance in the 680–2500 nm range,  $R_{\text{IR}}$  is ~83% (**Figure 1c**). The angle-dependent reflectance and transmittance spectra do not change appreciably as a function of incidence angle, at least up to 60° for unpolarized light (**Figure 1g**).

### Optical design of our cool window

**Figure 2a** shows the optical properties of the DMD structure (Ta<sub>2</sub>O<sub>5</sub> 40 nm/Ag 23 nm/Ta<sub>2</sub>O<sub>5</sub> 40 nm) alone, which is intended to reflect light at wavelengths longer than 1000 nm. The DMD lacks high reflectance in the wavelength ranges of 350–400 nm and 680–1000 nm. To address this limitation, we designed a modified Bragg reflector that features two photonic bandgaps on both sides of the visible spectrum, which we refer to as a dual-band selective reflector (DBSR). The DBSRs are implemented using a combination of planar SiO<sub>2</sub> and Ta<sub>2</sub>O<sub>5</sub> films.

The calculated  $T$  and  $R$  spectra of DBSRs as the number of SiO<sub>2</sub> (108 nm)/Ta<sub>2</sub>O<sub>5</sub> (112 nm) pairs are increased from 1 to 5 are shown in **Figure 2b,c**. The reflectance in the wavelength ranges of 350–400 nm and 680–950 nm increases with the number of pairs, while maintaining high visible transmittance. We would like to emphasize here that our DBSRs are somewhat different from distributed Bragg reflectors (DBRs) because conventional DBRs do not simultaneously achieve high  $R$  at the UV and near-IR ranges (350–400 nm and 680–950 nm); for example, **Figure 2d** shows the calculated  $R$  values of conventional DBRs with a target center wavelength of 780 nm. One pair is composed of SiO<sub>2</sub> (134 nm)/Ta<sub>2</sub>O<sub>5</sub> (94 nm), with each thickness corresponding to  $\lambda/4n$ , where  $\lambda$  is the wavelength of 780 nm and  $n$  is the refractive index ( $n_{\text{SiO}_2} = 1.45$  and  $n_{\text{Ta}_2\text{O}_5} = 2.08$  at 780 nm). The DBR spectra do not show high

$R$  in the UV range, while their spectra in the near-infrared are almost identical to those of our DBSRs (compare **Figure 2c** vs. **Figure 2d**).

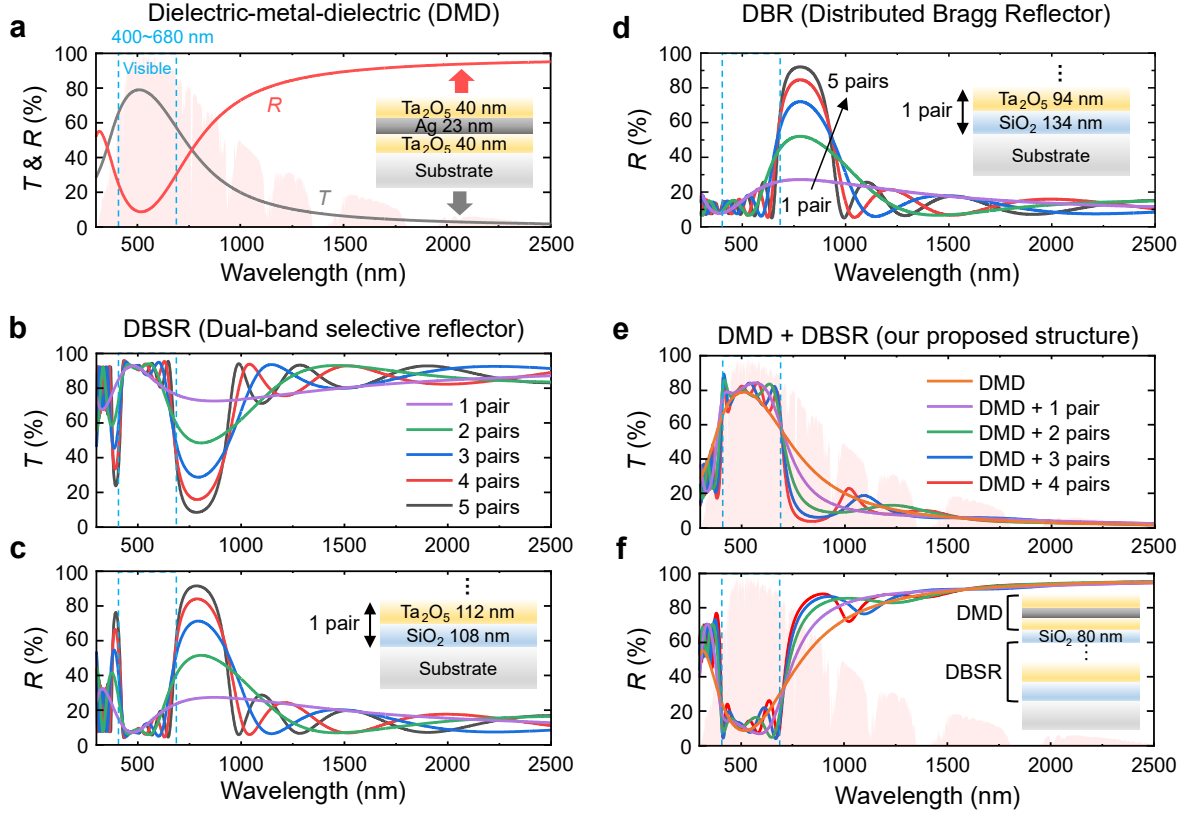


**Figure 2.** Calculated optical properties of our dielectric-metal-dielectric (DMD) structure, our dual-band selective reflectors (DBSRs), and reference distributed Bragg reflectors (DBRs) with different numbers of layers. **(a)** Calculated  $T$  and  $R$  spectra of the DMD structure (Ta<sub>2</sub>O<sub>5</sub> 40 nm/Ag 23 nm/Ta<sub>2</sub>O<sub>5</sub> 40 nm). **(b, c)** Calculated **(b)**  $T$  and **(c)**  $R$  spectra of our DBSRs, from 1 to 5 pairs. One pair corresponds to SiO<sub>2</sub> 108 nm/Ta<sub>2</sub>O<sub>5</sub> 112 nm. **(d)** Calculated  $R$  spectra of DBRs, from 1 to 5 pairs. One pair represents SiO<sub>2</sub> 134 nm/Ta<sub>2</sub>O<sub>5</sub> 94 nm. **(e, f)** Calculated **(e)**  $T$  and **(f)**  $R$  spectra of the integrated photonic structure, where the DMD is placed on top of a DBSR with different numbers of pairs. There is an 80-nm-thick SiO<sub>2</sub> intermediate layer as an optical spacer between the DMD and the DBSR.

To briefly explain the difference between conventional DBRs and our DBSRs, the thickness of DBRs ( $\lambda_{\text{target}}/4n$ ) is designed to produce constructive interference for reflected light, which occurs at  $\lambda_{\text{target}}/(2m-1)$ , where  $m$  is a positive integer. For example, for  $\lambda_{\text{target}} = 780$  nm, where the first high-reflectance mode ( $m = 1$ ) occurs, the second mode ( $m = 2$ ) appears at  $780/3 = 260$  nm. So, it is difficult to achieve high reflectance in both the 350–400 and 680–950 nm ranges using conventional DBRs.

However, we found that if the thickness deviates slightly from  $\lambda_{\text{target}}/4n$ , which results in imperfect constructive interference, the wavelengths of higher-order modes ( $m = 2, 3, \dots$ ) can be manipulated while maintaining the first mode near  $\sim 780$  nm. For example, the  $R$  spectra of DBSRs in **Figure 2c** show high  $R$  at the first mode around 780 nm and at the second mode

around 390 nm. See **Note S1** for detailed comparison of the basic working principles of DBRs and DBSRs.

To exploit the advantages of both the DMD and DBSRs, we stacked the DMD structure and the DBSRs (1–4 pairs), with an 80-nm-thick SiO<sub>2</sub> intermediate layer as an optical spacer. **Figure 2e** and **2f** show the calculated  $T$  and  $R$  spectra, respectively, of the combined structures, which show abrupt changes in  $T$  and  $R$  spectra around both 390 and 680 nm.

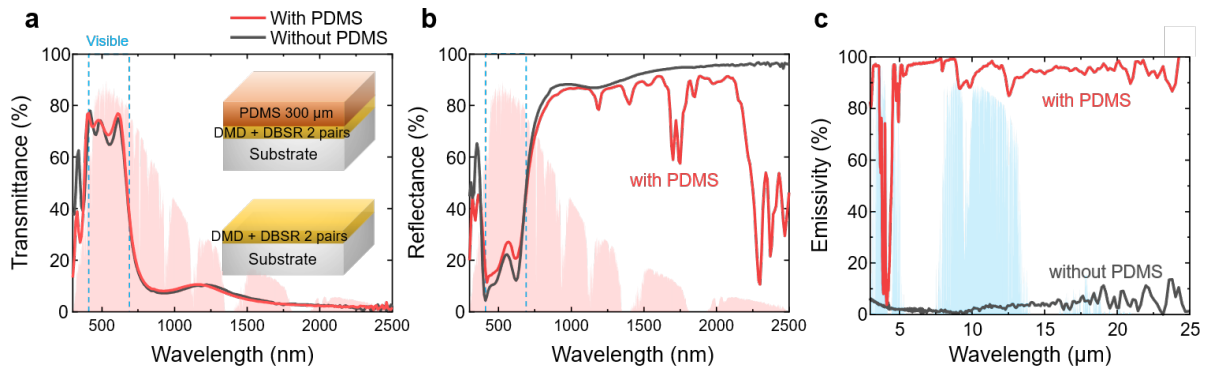


**Figure 3.** Measured optical properties with and without a thermal-emissive layer (300- $\mu\text{m}$ -thick PDMS) on the DBSR/DMD stack (Ta<sub>2</sub>O<sub>5</sub> 40 nm/Ag 23 nm/Ta<sub>2</sub>O<sub>5</sub> 40 nm/SiO<sub>2</sub> 80 nm/Ta<sub>2</sub>O<sub>5</sub> 112 nm/SiO<sub>2</sub> 108 nm/Ta<sub>2</sub>O<sub>5</sub> 112 nm/SiO<sub>2</sub> 108 nm/substrate). **(a–c)** Measured **(a)** transmittance, **(b)** reflectance, and **(c)** emissivity of the DBSR/DMD stack with and without the PDMS layer.

The 2-pair DBSR/DMD stack was fabricated, and **Figure 3** shows the measured transmittance, reflectance, and emissivity spectra. Due to the presence of the Ag layer, the DBSR/DMD stack has both very low transmittance and very low emissivity in the mid-infrared (**Figure 3c**). To significantly increase the emissivity (to facilitate radiative cooling of the window), we added a 300- $\mu\text{m}$ -thick PDMS layer on top because PDMS is visible-transparent, but highly emissive in the mid-infrared due to molecular vibrational resonances.<sup>15, 17</sup> The resulting cool window has an average emissivity ( $\epsilon$ ) of 94% in the 3–25  $\mu\text{m}$  range, while the DBSR/DMD stack alone has an average  $\epsilon$  lower than 5% (**Figure 3c**). The PDMS layer barely affects the  $T$  as shown in **Figure 3a**, but it does absorb in certain near-infrared wavelengths (**Figure 3b**). However, the portion of the solar energy in those ranges is small, so that does not significantly affect the performance of the cool window.

### Outdoor temperature experiment

To evaluate the cooling performance of our cool window, we conducted an outdoor temperature experiment on Oct 10, 2023, in Daejeon, South Korea, during the day. We prepared four polystyrene boxes ( $26 \times 26 \times 27 \text{ cm}^3$ ) with 2 cm thickness and cut a square hole ( $6.4 \times 6.4 \text{ cm}^2$ ) in the top of each box (**Figure 4a**). We painted the interiors of the boxes black to mimic the

interior of a vehicle and placed four thermocouples in each box to measure the air temperature (the thermocouples were suspended in air). The ambient temperature outside of the box was measured by a thermocouple under a polystyrene foam to avoid direct sunlight. We prepared four samples on 4-inch glass substrates: glass, glass/PDMS, glass/2-pair DBSR/DMD structure, and glass/2-pair DBSR/DMD/PDMS; in all cases, the PDMS layer was 300  $\mu\text{m}$  thick. We attached each of these samples directly below the holes in the boxes. The measured  $R$  and  $T$  spectra of the glass and glass/PDMS samples, spanning from the ultraviolet to mid-infrared range, are shown in **Note S2**. Finally, we placed a low-density polyethylene film on top of each hole to minimize convection.<sup>18</sup>

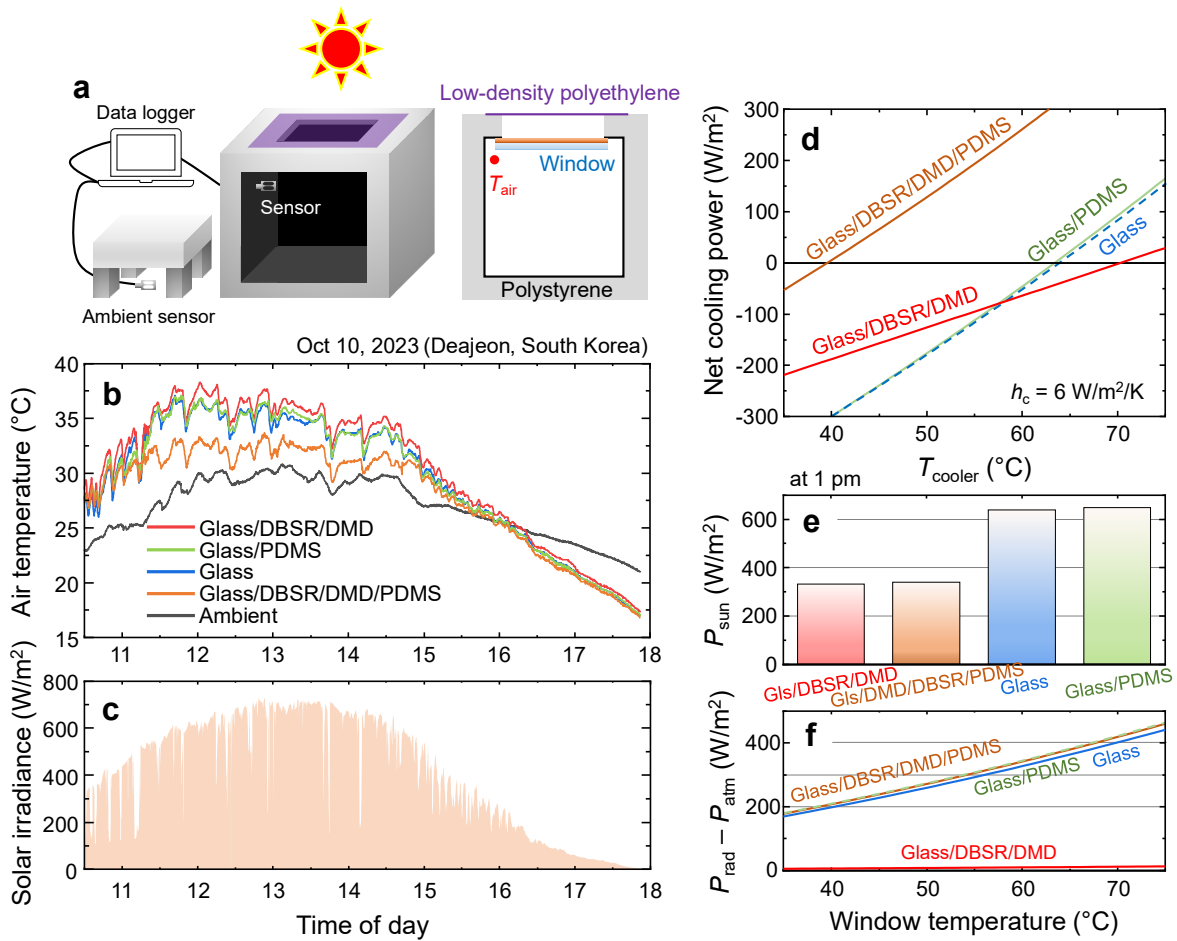


**Figure 4.** Outdoor temperature experiment. **(a)** Depiction of our outdoor experiment setup: four polystyrene boxes with a square hole on the top, painted black on the inside to mimic a vehicle. Each sample (glass, glass/PDMS, glass/DBSR (2-pair)/DMD, glass/DBSR (2-pair)/DMD/PDMS) was placed directly beneath the hole of each box, and a low-density polyethylene film was placed over the hole to minimize convection. An air temperature sensor was placed inside the box, avoiding direct sunlight, and suspended in air. An ambient temperature sensor was placed under a polystyrene foam to avoid direct sunlight. All four samples were measured simultaneously. **(b, c)** Measured air temperatures **(b)** and solar irradiance **(c)** of the four samples and the ambient temperature on October 10, 2023, at KAIST, in Daejeon, South Korea (36.27°N/127.36°E). Our cool window (glass/DBSR/DMD/PDMS) shows a temperature up to 3.8 °C lower than the glass sample, and 4.5 °C lower than the glass/DBSR/DMD without the PDMS layer. **(d)** Calculated net cooling power of the four samples as a function of the window temperature, including incident solar radiation and radiative and nonradiative cooling. **(e)** Calculated solar absorption in both the cool window, and inside the box ( $P_{\text{sun}}$  defined as  $715 \text{ W/m}^2 \times (1 - \text{reflectance})$

of the cool window)). **(f)** Calculated net radiative thermal flux,  $P_{\text{rad}} - P_{\text{atm}}$ , where  $P_{\text{rad}}$  represents the thermal radiation from the cooler and  $P_{\text{atm}}$  represents the atmospheric radiation absorbed by the cool window; this was calculated using our gradient atmospheric model<sup>19</sup>. Note that in (f), sunlight is not included.

**Figure 4b** shows the measured air temperature inside the box for the four different windows, along with the ambient temperature, while **Figure 4c** shows the measured solar irradiance. During the daytime, the cool window (glass/DBSR/DMD/PDMS) shows the lowest temperatures, up to 3.8 °C lower than the bare glass window.

**Figure 4d** shows the calculated net cooling power of each sample as a function of the window temperature. We used our recently reported gradient atmospheric model, which considers altitude-dependent atmospheric gas composition and temperature profiles<sup>19</sup>, to calculate the cooling power. Refer to ref. <sup>19</sup> and **Note S3** for details of the cooling power calculation. The equilibrium temperature, at which the net cooling power equals zero, is the lowest for the glass/DBSR/DMD/PDMS and highest for the glass/DBSR/DMD, showing good agreement with our experiment.

**Figure 4e** shows the solar absorption of the window and the black-painted box,  $P_{\text{sun}}$  defined as  $(1 - R) \times 715 \text{ W/m}^2$ ;  $715 \text{ W/m}^2$  is the solar irradiance at 1 pm. **Figure 4f** shows the net radiative thermal flux,  $P_{\text{rad}} - P_{\text{atm}}$ , where  $P_{\text{rad}}$  represents the power emitted from the window and  $P_{\text{atm}}$  represents the power emitted from the atmosphere and absorbed by the window (not accounting for sunlight). Although the solar absorption of the glass/DBSR/DMD and the glass/DBSR/DMD/PDMS samples are nearly identical (**Figure 4e**), the glass/DBSR/DMD/PDMS sample demonstrates higher performance because of its higher thermal emissivity (**Figure 4f**), resulting in a temperature drop up to 4.5 °C.

Note that in our experiments, all of the coatings were on the outside of the glass window. For this reason, the glass/DBSR/DMD sample results in higher air temperature inside, compared to the glass-only sample (**Figure 4b**), because even though the glass/DBSR/DMD film has solar transmittance  $\sim 300 \text{ W/m}^2$  lower than the glass-only sample, it also has much lower infrared emissivity. In our glass/DBSR/DMD/PDMS samples, the PDMS provides very high emissivity. However, the PDMS layer may not be necessary if the DBSR and DMD layers are coated on the inside of the glass rather than on the outside, since bare glass has relatively high emissivity; this configuration also makes it easier to protect the coatings against damage from the outside.

## Discussion

The ideal design of a window in a hot environment has slightly paradoxical needs; it needs to be transparent over the visible to provide visibility, but reflect as much sunlight as possible,

despite the fact that a lot of the solar spectrum is in and around the visible range. Our proposed solution is a highly transparent window across most of the visible (400-680 nm), which has sharp transitions in the spectrum to high reflectance in the ultraviolet and near-infrared, just outside of the visible range. We accomplish these sharp transitions using just 7 optical layers by combining a metal film for near-infrared reflectance with a special modified Bragg distributed reflector which has sharp peaks in both the near-infrared and the near-ultraviolet. Our fabricated cool window has high visible transparency ( $T_{\text{vis}} > 70\%$ ) while maintaining high reflectance in the ultraviolet ( $R_{\text{UV}} > 60\%$ ) and the near infrared ( $R_{\text{IR}} > 80\%$ ). The spectral features persist over a broad range of angles. We also added an additional PDMS layer on top to maximize mid-infrared emissivity and therefore maximize cooling of the window. Our cool window achieves an air temperature reduction of up to 3.8 °C compared to a reference piece of glass.

## Methods

*Sample Fabrication and optical characterization:* The oxide materials ( $\text{SiO}_2$  and  $\text{Ta}_2\text{O}_5$ ) were deposited using an electron-beam evaporator, and the Ag layer was deposited using a thermal evaporator; both evaporators were in the same chamber. The base pressure of the chamber was  $\sim 10^{-6}$  Torr. The deposition rate for the oxide materials was 2–3 Å/s, and  $\sim 3$  Å/s for the Ag layer.

Since the refractive index of a glass substrate ( $\sim 1.52$ ) is similar to that of  $\text{SiO}_2$  ( $\sim 1.46$ ), the bottom-most  $\text{SiO}_2$  layer of the DBSR was omitted in **Figure 1a**; instead, a  $\text{Ta}_2\text{O}_5$  layer is present as the bottom-most layer.

A mixture of PDMS and curing agent at a mass ratio of 8:2 was prepared and spin-coated at 500 rpm for 15 seconds. The PDMS-coated sample was then placed in a vacuum chamber for 15 minutes to remove air bubbles and form a dense film, followed by baking at 90 °C for 15 minutes.

The overall reflection and transmission spectra (300–2500 nm) were measured using a UV-visible spectrophotometer (Lambda 1050, PerkinElmer), and the emissivity spectra in the mid-IR region were measured using Fourier-transform infrared spectroscopy (Nicolet iN10MX, ThermoFisher).

*Optical calculations:* The overall calculated  $R$  and  $T$  spectra were obtained using the transfer matrix method. The refractive indices of  $\text{SiO}_2$  and  $\text{Ta}_2\text{O}_5$  were measured using an

ellipsometer, while that of Ag was extracted from the literature<sup>20</sup>. These are shown in **Figure S5**.

*Outdoor experiment:* The air temperatures inside the polystyrene boxes were measured using four K-type thermometers (Omega Engineering), connected with a temperature data logger (Omega Engineering, RDXL4SD). The ambient temperature was measured using a temperature sensor (Omega Engineering, RTD-805), which was placed under polystyrene foam with a hole, covered with aluminum foil, and connected to an external data logger (Omega Engineering, OM-CP-RTDTEMP101A). Solar irradiance was measured using a commercial photodiode (Thorlabs, S120VC) and calibrated using a solar simulator at 547.3 W/m<sup>2</sup>.

### **Supporting Information**

PDF file available online

### **Acknowledgements**

At KAIST, this work was supported by the Creative Materials Discovery Program through the National Research Foundation of Korea (NRF) funded by the Ministry of Science and ICT (NRF-2016M3D1A1900035). At UW-Madison, work was supported primarily by internal funding.

### **Author Contribution**

Y. Jin and S. Kim contributed equally to this work. Y. Jin and K. Yu conceived the concept of the work. Y. Jin designed the optical structures and performed the optical calculations. S. Kim fabricated the samples and conducted the overall experiments, with contributions from Y. Jin. Y. Jin and M. Kats performed the cooling power analysis using a gradient atmospheric model. Y. Jin and M. Kats wrote most of the paper, with contributions from all authors. K. Yu and M. Kats oversaw the research.

### **Conflict of Interest**

The authors declare no conflict of interest.

### **References**

- (1) I. Dadour; I. Almanjahie; N. Fowkes; G. Keady; K. Vijayan, Temperature variations in a parked vehicle. *Forensic Science International* **2011**, *207*, 205-211.
- (2) C. Schaefer; G. Bräuer; J. Szczyrbowski, Low emissivity coatings on architectural glass. *Surface Coatings Technology* **1997**, *93*, 37-45.

- (3) A. Al-Shukri, Thin film coated energy-efficient glass windows for warm climates. *Desalination* **2007**, *209*, 290-297.
- (4) G. K. Dalapati; S. Masudy-Panah; S. T. Chua; M. Sharma; T. I. Wong; H. R. Tan; D. Chi, Color tunable low cost transparent heat reflector using copper and titanium oxide for energy saving application. *Scientific Reports* **2016**, *6*, 20182.
- (5) K. Sibin; N. Selvakumar; A. Kumar; A. Dey; N. Sridhara; H. Shashikala; A. K. Sharma; H. C. Barshilia, Design and development of ITO/Ag/ITO spectral beam splitter coating for photovoltaic-thermoelectric hybrid systems. *Solar Energy* **2017**, *141*, 118-126.
- (6) T. Tani; S. Hakuta; N. Kiyoto; M. Naya, Transparent near-infrared reflector metasurface with randomly dispersed silver nanodisks. *Optics Express* **2014**, *22*, 9262-9270.
- (7) M. Van Nguyen; T. Okatani; Y. Kanamori, Fabrication of functional metamaterials for applications in heat-shielding windows and 6G communications. *Applied Optics* **2023**, *62*, 7411-7419.
- (8) Z. Zhou; X. Wang; Y. Ma; B. Hu; J. Zhou, Transparent polymer coatings for energy-efficient daytime window cooling. *Cell Reports Physical Science* **2020**, *1*.
- (9) X. Zhang; X. Li; F. Wang; W. Yuan; Z. Cheng; H. Liang; Y. Yan, Low - Cost and Large - Scale Producing Biomimetic Radiative Cooling Glass with Multiband Radiative Regulation Performance. *Advanced Optical Materials* **2022**, *10*, 2202031.
- (10) M. Bae; D. H. Kim; S.-K. Kim; Y. M. Song, Transparent energy-saving windows based on broadband directional thermal emission. *Nanophotonics* **2024**.
- (11) Y. Zhu; H. Luo; C. Yang; B. Qin; P. Ghosh; S. Kaur; W. Shen; M. Qiu; P. Belov; Q. Li, Color-preserving passive radiative cooling for an actively temperature-regulated enclosure. *Light: Science Applications* **2022**, *11*, 122.
- (12) S. Kim; W. Shang; S. Moon; T. Pastega; E. Lee; T. Luo, High-performance transparent radiative cooler designed by quantum computing. *ACS Energy Letters* **2022**, *7*, 4134-4141.
- (13) J. Kim; S. Baek; J. Y. Park; K. H. Kim; J. L. Lee, Photonic multilayer structure induced high near - infrared (NIR) blockage as energy - saving window. *Small* **2021**, *17*, 2100654.
- (14) M. Kim; D. Lee; S. Son; Y. Yang; H. Lee; J. Rho, Visibly transparent radiative cooler under direct sunlight. *Advanced Optical Materials* **2021**, *9*, 2002226.
- (15) Y. Jin; Y. Jeong; K. Yu, Infrared - Reflective Transparent Hyperbolic Metamaterials for Use in Radiative Cooling Windows. *Advanced Functional Materials* **2023**, *33*, 2207940.
- (16) The National Highway Traffic Safety Administration.  
<https://www.nhtsa.gov/interpretations/nht87-349>.  
<https://www.nhtsa.gov/interpretations/nht87-349#:~:text=205%20requires%2070%25%20light%20transmittance,if%20used%20for%20driving%20visibility> (accessed October 10, 2025).
- (17) L. Zhou; H. Song; J. Liang; M. Singer; M. Zhou; E. Stegenburgs; N. Zhang; C. Xu; T. Ng; Z. Yu, et al., A polydimethylsiloxane-coated metal structure for all-day radiative cooling. *Nature Sustainability* **2019**, *2*, 718-724.
- (18) A. P. Raman; M. A. Anoma; L. Zhu; E. Rephaeli; S. Fan, Passive radiative cooling below ambient air temperature under direct sunlight. *Nature* **2014**, *515*, 540-544.
- (19) Y. Jin; M. A. Kats, A gradient atmospheric model reveals enhanced radiative cooling potential and demonstrates the advantages of broadband emitters. *arXiv* **2024**, *2406.00572*.
- (20) A. D. Rakić; A. B. Djurišić; J. M. Elazar; M. L. Majewski, Optical properties of metallic films for vertical-cavity optoelectronic devices. *Applied Optics* **1998**, *37*, 5271-5283.

# Supporting Information

## **Cool windows: simultaneously engineering high visible transparency and strong solar rejection**

*Yeonghoon Jin,<sup>1,2,#</sup> Seungwon Kim,<sup>1,#</sup> Tanuj Kumar,<sup>2</sup> Mikhail A. Kats,<sup>2\*</sup> and Kyoungsik Yu<sup>1,\*</sup>*

<sup>1</sup>School of Electrical Engineering, Korea Advanced Institute of Science and Technology (KAIST), Daejeon 34141, Republic of Korea

<sup>2</sup>Department of Electrical and Computer Engineering, University of Wisconsin-Madison, Madison, WI 53706, USA

<sup>#</sup>These authors contributed equally

E-mail: [mkats@wisc.edu](mailto:mkats@wisc.edu), [ksyu@kaist.edu](mailto:ksyu@kaist.edu)

## Note S1. Distributed Bragg reflectors (DBRs) and our dual-band selective reflectors (DBSRs)

This section introduces the concept of a dual-band selective reflector (DBSR), which is a modified version of a distributed Bragg reflector (DBR), but where we can independently control the wavelengths of multiple reflection peaks. For this paper, we aim to simultaneously design reflectance peaks in the near-IR and near-UV.

DBRs create constructive interference of partially reflected waves (**Figures S1a,b**, though note that in this figure we only draw the primary partial reflections, neglecting multiple reflections within each film; this is a reasonable assumption assuming that the Fresnel reflection coefficients at each interface are not too high).<sup>1</sup>

**Figure S1a** shows the reflection phase shift ( $\phi$ ) of the partial reflected waves (from  $r_1$  to  $r_4$ ) in a DBR, and **Figure S1b** shows the sum of the complex-reflectance partial waves of a DBR composed of 5 pairs of SiO<sub>2</sub>/Ta<sub>2</sub>O<sub>5</sub>. Here, the target wavelength ( $\lambda_{\text{target}}$ ) for the center of the photonic bandgap is 780 nm, and SiO<sub>2</sub> is used as the low-index material ( $L$ ) and Ta<sub>2</sub>O<sub>5</sub> as the high-index material ( $H$ ); the thickness of Ta<sub>2</sub>O<sub>5</sub> is 94 nm and that of SiO<sub>2</sub> is 134 nm, which corresponds to  $\lambda_{\text{target}}/4n$ , where  $n$  is the refractive index. The amplitude of the sum of the overall reflected waves ( $r_{\text{total}}$ ) approaches 1, and its phase is  $\pi$ .

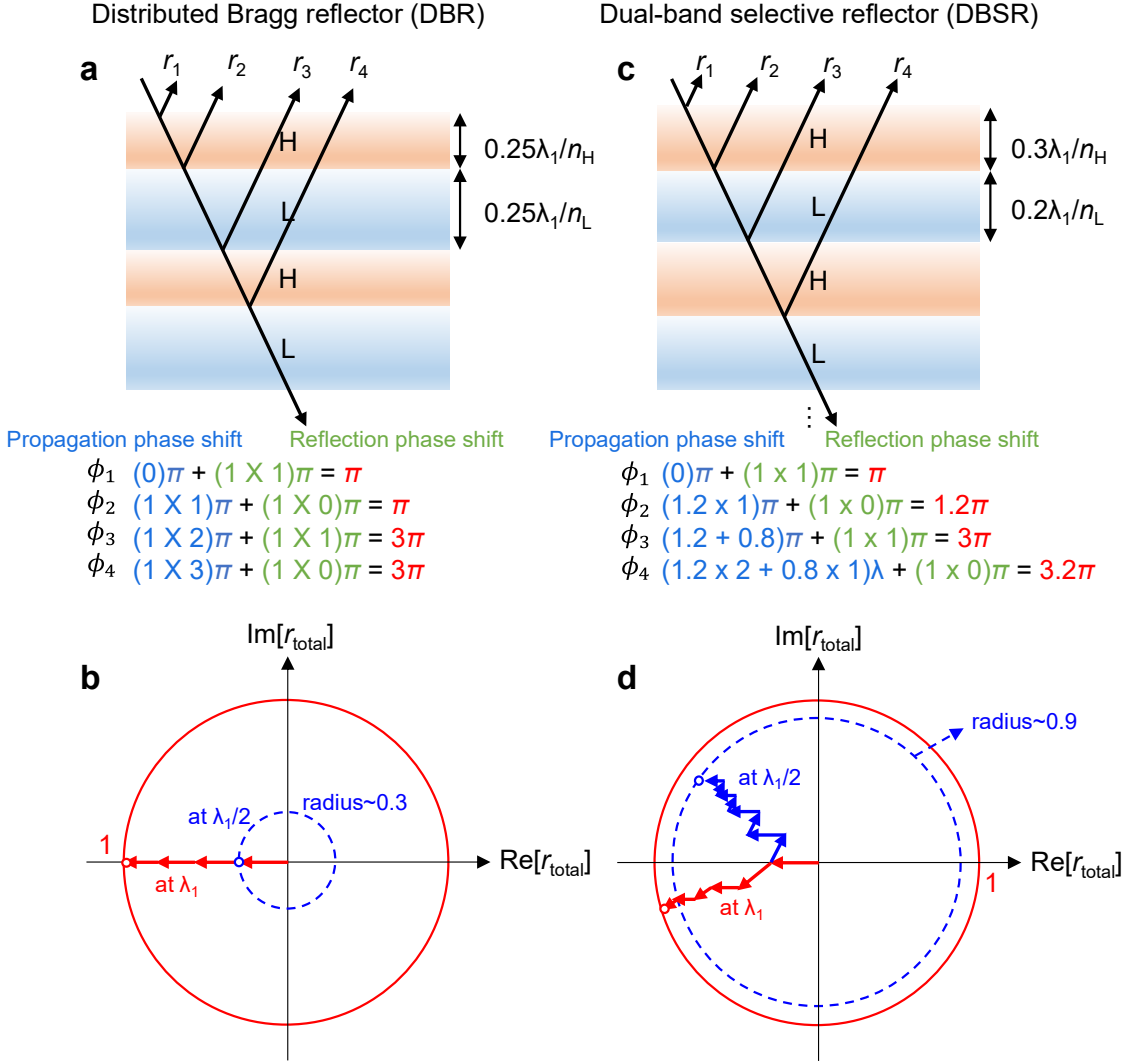


**Figure S1.** Working principles of a conventional distributed Bragg reflector (DBR) and our dual-band selective reflector (DBSR). **(a,c)** Depiction of partial reflected waves of **(a)** a DBR and **(c)** a DBSR, neglecting multiple reflections within the films. The total accumulated phase comprises the round-trip propagation phase and reflection phase. **(b,d)** Visual sum of the partial reflected waves of **(b)** a 5-pair DBR and **(d)** a 5-pair DBSR, both at  $\lambda_1 = 780$  nm. In both cases,  $\text{SiO}_2$  ( $n_L = 1.46$ ) is used as the low-index material and  $\text{Ta}_2\text{O}_5$  ( $n_L = 2.08$ ) as the high-index material.

To achieve total constructive interference, the reflected waves must be in phase. The reflection at the top interface  $\phi_1$  (air to high index) introduces a phase shift of  $\pi$ , and thus, the phase of subsequent reflected waves ( $\phi_2, \phi_3, \phi_4 \dots$ ) must have phase of  $\pi, 3\pi, 5\pi, 7\pi$ , etc.

For example, the reflection phase shift of the second interface,  $\phi_2$ , is 0 (high to low index), and therefore, the round-trip propagation phase shift within the topmost layer must be an odd multiple of  $\pi$ . For the phase shift at the next interface  $\phi_3$ , the reflection phase shift (from low to high index) is  $\pi$ , so the round-trip propagation phase shift (in the first and second layers) should

be an even multiple of  $\pi$ . Thus, the required round-trip propagation phase alternates between odd and even multiple of  $\pi$  (see the phase calculations in **Figure S1a**). To satisfy this, the round-trip propagation phase shift in a single layer must be an odd multiple of  $\pi$ . This condition can be written as:

$$2knd = (2m - 1)\pi, \quad (\text{S1})$$

where  $k$  is the wavenumber ( $k = 2\pi/\lambda_m$ ),  $n$  is the refractive index,  $d$  is the thickness, and  $m$  is a positive integer.<sup>1</sup> For the first mode ( $m = 1$ ), the thickness  $d$  should be  $\lambda_1/4n$ . Provided that the refractive index of Ta<sub>2</sub>O<sub>5</sub> is 2.08 and that of SiO<sub>2</sub> is 1.45, the corresponding thickness of Ta<sub>2</sub>O<sub>5</sub> is  $\sim 94$  nm and that of SiO<sub>2</sub> is  $\sim 134$  nm. When  $n$  and  $d$  are fixed, **Equation S1** is satisfied when  $\lambda_m = 4nd/(2m - 1)$ . For example, when  $\lambda_1 = 4nd = 780$  nm,  $\lambda_2 = 4nd/3 = \lambda_1/3 = 260$  nm and  $\lambda_3 = 4nd/4 = \lambda_1/4 = 156$  nm. Accordingly, realizing high  $R$  in both the 300–400 nm and 680–950 nm ranges is not possible this structure; the reflection amplitude is  $\sim 1$  at  $\lambda_1 = 780$  nm, whereas that at  $\lambda_1/2 = 390$  nm is  $\sim 0.3$  (**Figure S1b**).

Here, we design a structure to adjust wavelengths of high-order modes ( $m = 2, 3, \dots$ ), while maintaining the wavelength and magnitude of the peak reflectance for the first mode. The idea is to slightly change the thickness from each layer from the  $0.25\lambda_1/n$  condition, while having the round-trip phase shift in one pair remain  $2\pi$  (**Figure S1c**). For example, let us assume that the thickness of the high-index layer is  $0.3\lambda_1/n_H$  ( $d_H = 112$  nm, where  $\lambda_1 = 780$  nm) and that of the low-index layer is  $0.2\lambda_1/n_L$  ( $d_L = 108$  nm). Then, the round-trip propagation phase shift of the high-index layer is  $1.2\pi$  ( $2 \times 0.3\lambda_1/n_H$ ) and that of the low-index is  $0.8\pi$  ( $2 \times 0.2\lambda_1/n_L$ ), and then the accumulated phases of the odd-numbered reflected waves ( $\phi_1 = \pi$ ,  $\phi_3 = 3\pi$ , and  $\phi_5 = 5\pi$ ) remain the same as in the DBR case (compare **Figure S1a** and **Figure S1c**), while the accumulated phase of the even-numbered reflections are slightly off (by  $0.2\pi$ ) from ideal constructive interference. Nevertheless, the total reflectance  $|r_{\text{total}}|$  at  $\lambda_1$  remains close to 1 (**Figure S1d**). The phase condition of this structure can be expressed as  $2kn_H d_H + 2kn_L d_L = 2m\pi$ , which simplifies to  $n_H d_H + n_L d_L = 0.5m\lambda_m$  ( $n_H d_H \neq n_L d_L \neq 0.25m\lambda_m$ ). Given that the left term is a constant, the higher-order modes appear at  $\lambda_2 = 780/2 = 390$  nm ( $m = 2$ ) and  $\lambda_3 = 780/3 = 260$  nm. This indicates that high reflectance can be achieved around 390 nm (ultraviolet) and 780 nm (near-infrared). See the reflected wave trajectories at  $\lambda_1 = 780$  nm and  $\lambda_1/2 = 390$  nm, in **Figure S1d**, which shows high reflection amplitude for both wavelengths. See **Figure 2c** in the main text for the reflectance spectra of the 5-pair DBSR.

The peak wavelength slightly shifts as the number of pair increases because of imperfect constructive interference, but the  $R$  values in the 350–400 and 680–950 nm wavelength ranges remain high. Note that if the round-trip propagation phase shift in each layer ( $2kn_Hd_H$  and  $2kn_Ld_L$ ) deviates too far from  $\pi$ , the imperfect constructive interference will significantly reduce the reflectance (**Figure S2**).

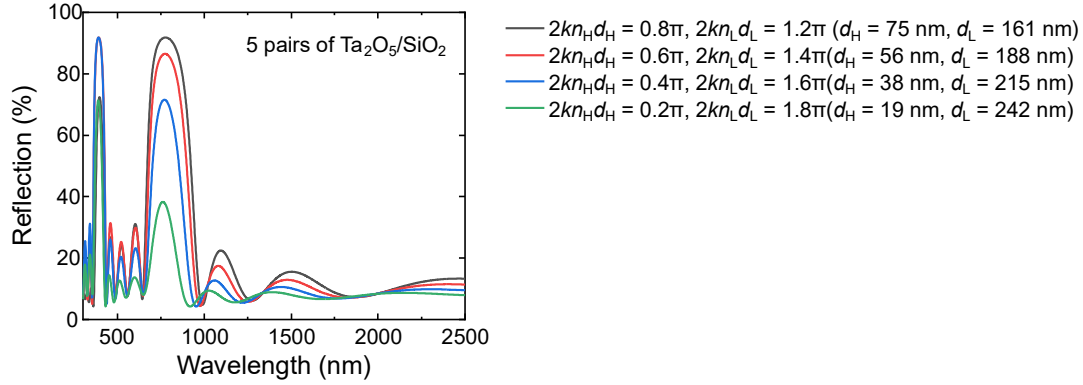


**Figure S2.** Reflection spectra of DBSRs with various thickness combinations (5 pairs).

In **Figure S3**, we compared the reflectance of the 6-pair DBR ( $\text{Ta}_2\text{O}_5$  94 nm/ $\text{SiO}_2$  134 nm) and the 6-pair DBSR ( $\text{Ta}_2\text{O}_5$  112 nm/ $\text{SiO}_2$  108 nm). Unlike the DBR, the DBSR shows high  $R$  in the 350–400 nm range, while there is almost no difference between the two in the 680–950 nm range.

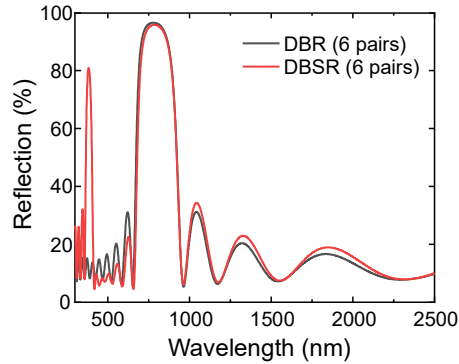


**Figure S3.** The reflection spectrum of the 6-pair DBR and the 6-pair DBSR.

## Note S2. Optical properties of samples and refractive indices of materials

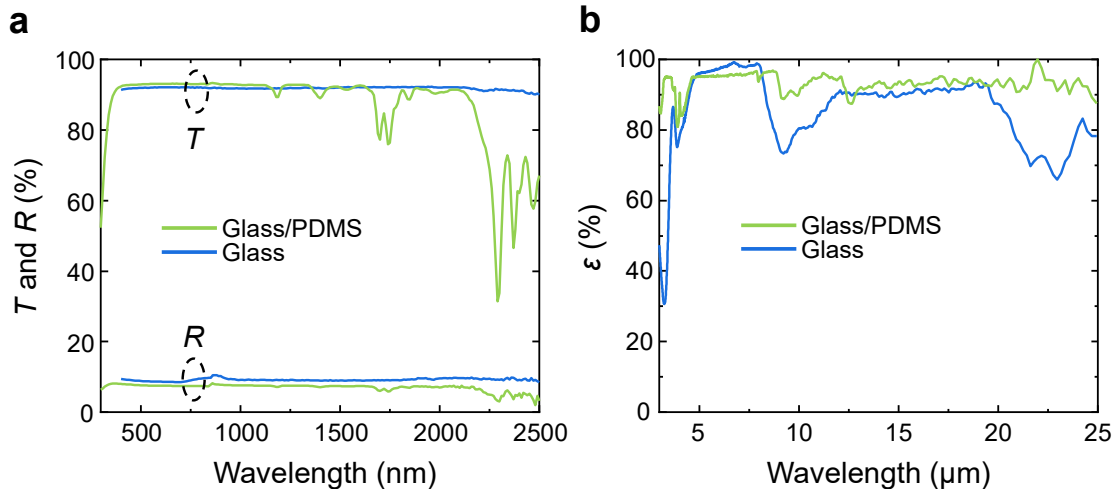


**Figure S4.** Optical properties of the glass and glass/PDMS (300  $\mu\text{m}$ ) samples. **(a)** Measured UV, visible, and near-IR transmittance ( $T$ ) and reflectance ( $R$ ), and **(b)** mid-infrared emissivity ( $\epsilon$ ) of both samples.

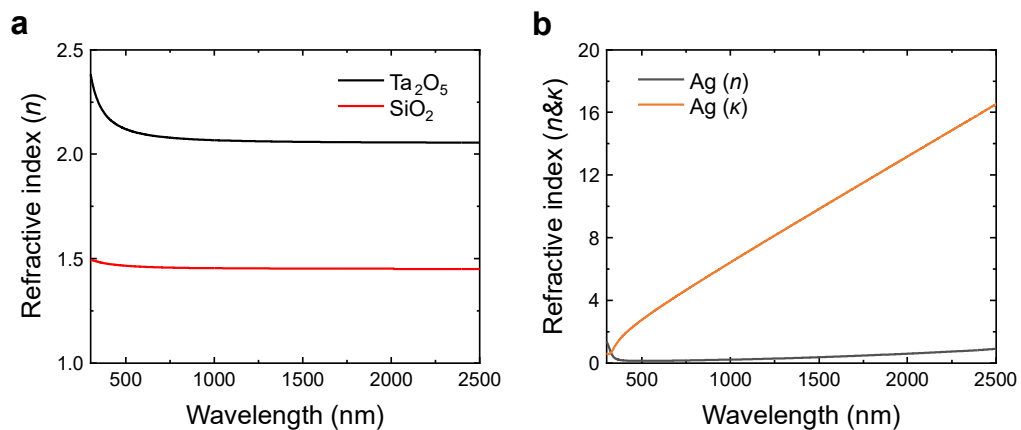


**Figure S5.** **(a)** The refractive indices of  $\text{Ta}_2\text{O}_5$  and  $\text{SiO}_2$  that were measured by an ellipsometer. **(b)** The complex refractive index of Ag that was extracted from the literature.<sup>2</sup>

### Note S3. A gradient atmospheric model to calculate the cooling performance

We recently demonstrated quantitatively that radiative cooling performance is significantly affected by altitude-dependent atmospheric gas composition and temperature, as well as by location and date/time.<sup>3</sup> However, most published papers have analysis that assumes a uniform atmosphere, where atmospheric gas composition and temperature are constant with respect to altitude. In reality, these parameters vary with altitude, and we found that the uniform atmospheric model typically underestimates cooling power by 10–40% compared to a gradient atmospheric model.<sup>3</sup> Here we summarize the relevant cooling calculations, the result of which is in **Figure 4(d-f)** in the main text.

Within the gradient atmospheric model, the net cooling power ( $P_{\text{cool}}$ ) can be written as:<sup>3</sup>

$$P_{\text{cool}} = P_{\text{rad}}(T_{\text{surface}}) - \sum_{n=1}^{n_{\text{atm}}} P_{\text{atm}}^n(T_{\text{atm}}^n) - P_{\text{sun}} - P_{\text{con}}(T_{\text{surface}}, T_{\text{atm},1}). \quad (\text{S2})$$

$P_{\text{rad}}$  is the power radiated from a cooling surface (here, the surface of our cool window), and can be written as:

$$P_{\text{rad}}(T_{\text{surface}}) = \int d\Omega \cos \theta \int_0^{\infty} d\lambda I_{\text{BB}}(T_{\text{surface}}, \lambda) \varepsilon_{\text{surface}}(\lambda, \theta), \quad (\text{S3})$$

where  $T_{\text{surface}}$  is the surface temperature,  $\int d\Omega = 2\pi \int_0^{\pi/2} d\theta \sin \theta$ ,  $\theta$  is the emission angle,  $I_{\text{BB}}$  is the spectral radiance of a blackbody, and  $\varepsilon_{\text{surface}}$  is the thermal emissivity of the surface. Here, the integration wavelength range is from 3 to 25  $\mu\text{m}$ .

The second term represents the power radiated from the atmosphere and then absorbed by the surface (here, the window). Since atmospheric gas composition and temperature vary with altitude, our gradient model accounts for this by dividing the atmosphere into 10 layers; the partial atmospheric emissivity ( $\varepsilon_{\text{atm}}$ ) from each atmospheric layer is shown in **Figure S6c**, with the temperature of each layer detailed in the figure caption.  $P_{\text{atm}}^n$  in the second term represents the power radiated from the  $n^{\text{th}}$  atmospheric layer and then absorbed by the cooler.  $P_{\text{atm}}^1$  can be given by:<sup>3</sup>

$$P_{\text{atm}}^1(T_{\text{atm}}^1) = \int d\Omega \cos \theta \int_0^{\infty} d\lambda I_{\text{BB}}(T_{\text{atm}}^1, \lambda) \varepsilon_{\text{surface}}(\lambda, \theta) \varepsilon_{\text{atm}}^1(\lambda, \theta), \quad (\text{S4})$$

where  $T_{\text{atm}}^1$  is the temperature of the first atmospheric layer (290 K at 0–0.5 km), and  $\varepsilon_{\text{atm}}^1$  is the emissivity of the first atmospheric layer.  $P_{\text{atm}}^n$  can be given by ( $n > 1$ ):<sup>3</sup>

$$P_{\text{atm}}^n(T_{\text{atm}}^n) = \int d\Omega \cos \theta \int_0^{\infty} d\lambda I_{\text{BB}}(T_{\text{atm}}^n, \lambda) \varepsilon_{\text{surface}}(\lambda, \theta) [\varepsilon_{\text{atm}}^n(\lambda, \theta) - \varepsilon_{\text{atm}}^{n-1}(\lambda, \theta)], \quad (\text{S5})$$

and the atmospheric temperatures of each layer ( $T_{\text{atm}}^n$ ) is shown in the caption of **Figure S6**.

The solar absorption can be given by:  $P_{\text{sun}} = \int_0^{\infty} d\lambda [1 - R_{\text{surface}}(\lambda, \theta_{\text{sun}})] I_{\text{Solar}}(\lambda)$ , where  $\theta_{\text{sun}}$  is the polar angle of the sun (in our case  $\theta_{\text{sun}} = 0$ , where the sun is directly shining on the window surface), and  $I_{\text{Solar}}$  is the AM1.5 solar spectrum.<sup>4</sup> We assumed that, in our experiment, the incident solar energy to the polystyrene boxes is entirely absorbed by the black-painted boxed. The non-radiative heat exchange via conduction and convection can be given by:  $P_{\text{con}} = h_c(T_{\text{atm}}^1 - T_{\text{cooler}})$ , where  $h_c$  is a heat transfer coefficient.

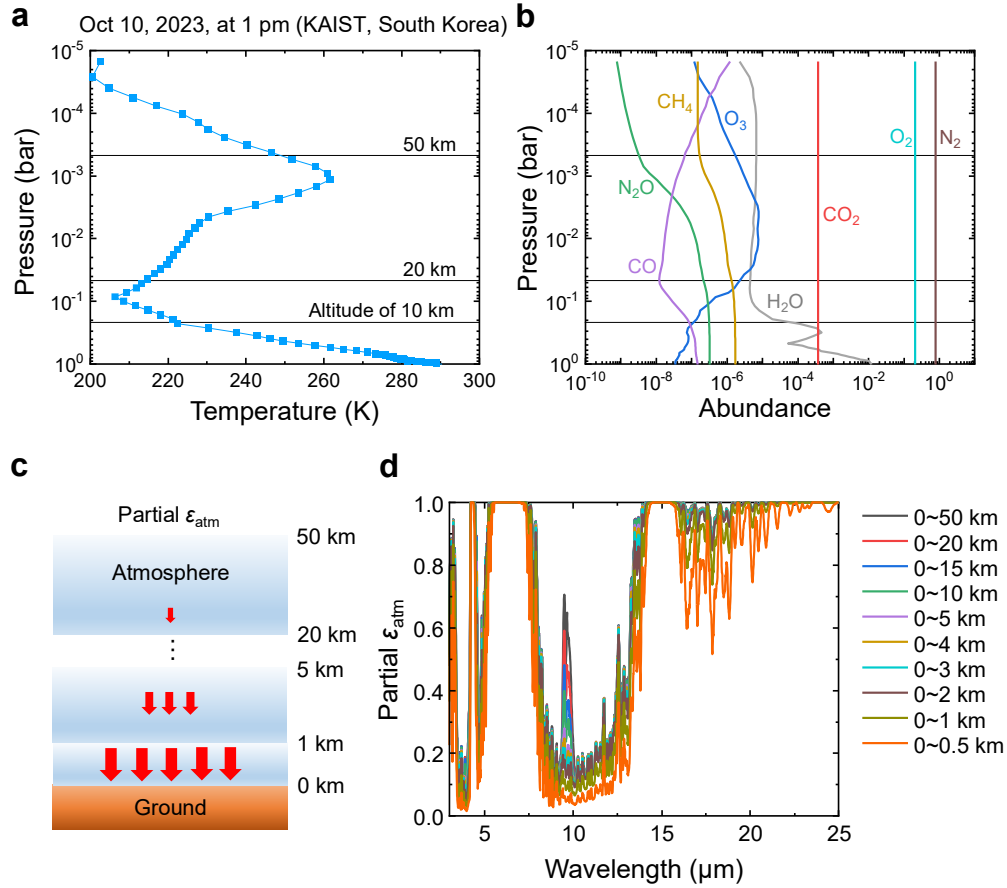


**Figure S6.** Altitude-dependent atmospheric information on October 10, 2023, at 1 pm at KAIST (36.37°N, 127.36°E). **(a)** Altitude-dependent atmospheric temperature profile. The y-axis represents both altitude and pressure. **(b)** Altitude-dependent atmospheric gas composition. The abundance indicates the ratio of the pressure of each gas to the total pressure at a given altitude. **(c)** Illustration of partial atmospheric emissivity ( $\epsilon_{\text{atm}}$ ). **(d)** Partial atmospheric emissivity ( $\epsilon_{\text{atm}}$ ) from 10 atmospheric layers. Most atmospheric radiation occurs from the first few kilometers above the ground, as the atmospheric gases are concentrated in this range. The atmospheric temperatures for each atmospheric layer, in order from the lowest altitude ( $T_{\text{atm},1}$ ) to the highest altitude ( $T_{\text{atm},10}$ ), are: 290, 286.3, 280.7, 275.9, 270, 262, 253.6, 220, 208, and 214 K.

**Figure S6a** shows the altitude-dependent atmospheric temperature profile at KAIST, South Korea (36.37°N, 127.36°E) on October 10<sup>th</sup>, 2023, at 1 pm; this is the time of the experiment in **Figure 4**. The atmospheric data was obtained through NASA's Planetary Spectrum Generator (PSG);<sup>5</sup> refer to our recent paper<sup>3</sup> for instructions on how to use the PSG. **Figure S6b** shows the altitude-dependent atmospheric gas abundance on the same date/time. The gas abundance ( $x$ -axis) indicates the ratio of the pressure of each gas to the total gas pressure at a given altitude; for example, the abundance of CO<sub>2</sub>, O<sub>2</sub>, and N<sub>2</sub> is maintained across the entire altitude, but their pressure indeed decreases with increasing altitude because the total pressure ( $y$ -axis) decreases. Note that H<sub>2</sub>O and CO<sub>2</sub> are concentrated in the first few kilometers from the ground, indicating that most thermal emission from the atmosphere occurs within a few kilometers from the ground.

## Reference

- (1) N. Kaiser; H. K. Pulker, *Optical interference coatings*; Springer, 2013; Vol. 88.
- (2) A. D. Rakić; A. B. Djurišić; J. M. Elazar; M. L. Majewski, Optical properties of metallic films for vertical-cavity optoelectronic devices. *Applied Optics* **1998**, *37*, 5271-5283.
- (3) Y. Jin; M. A. Kats, A gradient atmospheric model reveals enhanced radiative cooling potential and demonstrates the advantages of broadband emitters. *arXiv* **2024**, 2406.00572.
- (4) The American Society for Testing and Materials (ASTM) G-173 spectrum <https://www.nrel.gov/grid/solar-resource/spectra-am1.5.html>. (accessed June 05, 2025).
- (5) Planetary Spectrum Generator (PSG). <https://psg.gsfc.nasa.gov/>. (accessed March 03, 2025).